Macroscopic Ultralight Aerogel Monoliths of Imine-based Covalent Organic Frameworks

Jesús Á. Martín-Illán,[a] David Rodríguez-San-Miguel,[a] Oscar Castillo,[b,c] Garikoitz Beobide,[b,c] Javier Perez-Carvajal,[d] Inhar Imaz,[e] Daniel Maspoch[e,f,*] and Félix Zamora[a,g,h,i,*]

[a] Jesús Á. Martín-Illán, Dr. David Rodríguez-San-Miguel, Prof. Félix Zamora
Departamento de Química Inorgánica
Universidad Autónoma de Madrid
28049 Madrid, Spain
E-mail: felix.zamora@uam.es
[b] Dr. Oscar Castillo, Dr. Garikoitz Beobide
Departamento de Química Inorgánica
Universidad del País Vasco (UPV/EHU),
Apartado 644, 48080 Bilbao, Spain
[c] Dr. Oscar Castillo, Dr. Garikoitz Beobide
Basque Ctr Mat Applicat & Nanostruct (BCMat)
Universidad del País Vasco UPV/EHU
Leioa 48940, Spain
[d] Dr. Javier Perez-Carvajal
Laboratoire de Physique de l'Ecole Normale Supérieure, ENS
Université PSL, CNRS
Sorbonne Université, Paris, France
[e] Dr. Inhar Imaz, Prof. Daniel Maspoch
Catalan Institute of Nanoscience and Nanotechnology (ICN2), CSIC and BIST
Campus UAB
Bellaterra, 08193 Barcelona, Spain
E-mail: daniel.maspoch@icn2.cat
[f] Prof. Daniel Maspoch
ICREA
Pg. Lluís Companys 23, Barcelona, 08010, Spain
[g] Prof. Félix Zamora
Instituto Madrileño de Estudios Avanzados en Nanociencia (IMDEA-Nanociencia)
Cantoblanco, Madrid E-28049, Spain
[h] Prof. Félix Zamora
Institute for Advanced Research in Chemical Sciences (IAdChem)
Universidad Autónoma de Madrid. 28049 Madrid, Spain
[i] Prof. Félix Zamora
Condensed Matter Physics Center (IFIMAC)
Universidad Autónoma de Madrid. 28049 Madrid, Spain

Supporting information for this article is given via a link at the end of the document

Abstract: The use of covalent organic frameworks (COFs) in practical applications demands shaping them into macroscopic objects, which remains challenging. Herein, we report a simple three-step method to produce COF aerogels, based on sol-gel transition, solvent-exchange, and supercritical CO_2 drying, in which 2D imine-based COF sheets link together to form hierarchical porous structures. The resultant COF aerogel monoliths have extremely low densities (*ca*. 0.02 g cm^{-3}), high porosity (total porosity values of *ca*. 99 %), and mechanically behave as elastic materials under a moderate strain (< 25-35 %) but become plastic under greater strain. Moreover, these COF aerogels maintain the micro- and meso-porosity of their constituent COFs, and show excellent absorption capacity (*e.g.* toluene uptake: 32 g g^{-1}), with high removal efficiency (*ca*. 99 %). Finally, we show that the same three-step method can be used to create functional composites of these COF aerogels with nanomaterials. We hope that our new procedure paves the way to a wider variety of macroscopic COF-based aerogels.

Introduction

Practical applications that involve adsorption of gaseous or liquid molecules can be made cheaper and more efficient by optimizing the porous materials employed.[1] In the past decade, the interest in 2D porous structures has increased, owing to their intrinsically porous designed structures.[2] These include covalent organic frameworks (COFs),[3] crystalline porous organic polymers assembled by connecting organic building blocks through dynamic covalent bonds via reticular chemistry, which allows for a high degree of structural and functional customization.[4] Given their outstanding physicochemical properties,[5] high crystallinity, and permanent porosity with large surface areas, COFs have demonstrated great potential for applications[6] such as energy storage,[7] catalysis,[8] molecular storage, and water-purification/desalinization.[1a]

However, the typical products of COF syntheses are normally powders, rather than macroscale objects, thus limiting their practical use. To overcome this problem, different methodologies have recently been developed for shaping COFs into macroscopic porous objects such as monoliths, thin-films, and membranes.[1b, 9] Among them, there is particular interest in the possibility of shaping COFs into macroscopic hierarchically-porous objects that would contain a combination of pores of different size scales, as such objects would facilitate mass transport through the shaped material, enhancing the accessibility of the adsorbed molecules to the resultant COF intrinsic micro- and meso-pores.[10] Thus far, however, fabrication of these macroscopic porous objects is not straightforward, as their formation usually implies the total or partial collapse of the COF porosity. For instance, this occurs in three-dimensional

(3D) structures with hierarchical porosity produced by co-polymer synthesis, printing, or templating.[11] Interestingly, Banerjee *et al*.[12] have recently developed a gas-foaming method to produce COF foams of multiscale porosity. In their method, the reaction of sodium bicarbonate with an excess of *p*-toluene sulfonic acid leads to the continuous effervescence of CO_2, enabling the generation of COF foams. Remarkably, these foams showed hierarchical macro-, meso- and micro-porosity, allowing the ultrafast and efficient adsorption of various pollutants and micro-pollutants from water at very low concentrations.

Another class of very interesting macroscopic hierarchically porous objects is aerogels, porous materials with 3D hierarchical morphology and porosity, low densities, high surface areas, and high total pore volumes, all of which greatly facilitate mass transport of adsorbed molecules through their matrices. Aerogels are extremely important for several applications, including heterogeneous catalysis, energy storage, sensors, pollutant capture, and gas storage.[13],[14] They are traditionally prepared from silica gels,[15] but also can be made from metal oxides,[16] organic polymers,[17] carbon-based materials,[13] biopolymers,[18] even metal-organic frameworks,[19] and polyhedral.[20] However, to date, COF-based aerogels have been fabricated only via encapsulation of COF particles into aerogels made from other materials, such as alginate and graphene oxide. For instance, monolithic alginate aerogels incorporating different COFs have been fabricated using a freeze-drying template approach.[21] For Pd-based catalytic dehalogenation of chlorobenzene, these monolithic aerogels exhibit an excellent yield, with no aggregation or leaching of Pd after the recycling process. Also, a composite aerogel made of COF and reduced graphene oxide (rGO) has been recently reported.[22] This COF@rGO aerogel was also prepared using freeze-drying once the composite had been hydrothermally synthesized. It presents a high absorption capacity for organic solvents. Moreover, as a supercapacitor device running over 5000 cycles, it shows a capacitance performance of 269 F g^{-1} at 0.5 A g^{-1}, owing to its hierarchical structure, which favors rapid solvent-absorption, rapid charge-transfer, and ion-diffusion.

Herein, we report the preparation of a series of ultralight monolithic aerogels made from pure imine-based COFs, through a straightforward three-step method (Scheme 1). Three COF aerogels are synthesized using this method, in which a COF gel is first prepared by a sol-gel process under mild conditions. Then, this COF gel undergoes solvent exchange, and finally, it is dried under supercritical CO_2 ($scCO_2$). The COF aerogels exhibit a 3D sponge-like architecture built up from the interconnection of fiber-like structures made of assembled COF-nanosheets. The resultant monolithic COF aerogels maintain the micro- and meso-porosity of the constituent COF, and show unprecedented low densities (*ca*. only three times the density of air), interesting mechanical properties, and a hierarchical porous structure that features both meso- and macro-porosity.

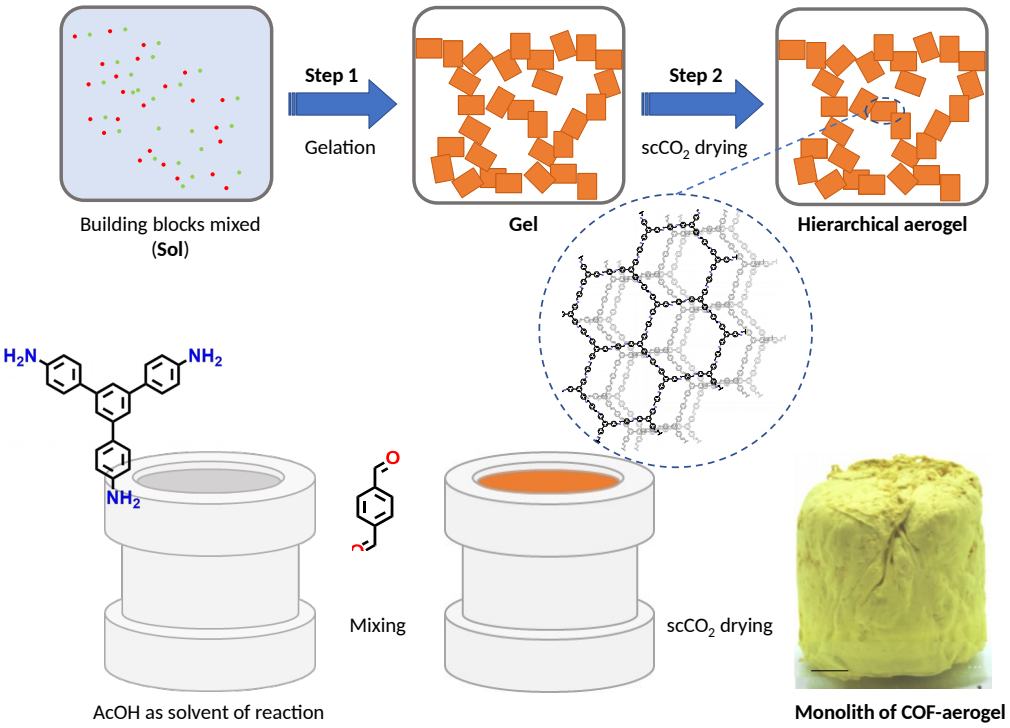

Scheme 1. Top: Schematic of the synthesis of hierarchical COF aerogels via sol-gel processes, comprising: i) mixture of the molecular building blocks in AcOH; ii) formation of the COF gels; and iii) solvent exchange and supercritical CO_2 activation. Bottom: Representation of the COF aerogel synthesis followed in this work, using TAPB-BTCA-AGCOF (photograph) as representative example of a macroscopic aerogel monolith. Scale bar: 0.5 cm.

As a proof-of-concept, we demonstrated that these monolithic COF aerogels could serve as reusable scavengers of toluene from contaminated water, for which they exhibit high removal efficiency (*ca*. 99 %). Additionally, we proved that the kinetic control over the sol-gel process enables the encapsulation of nanoparticles through ready modification of COF aerogel features, based on the exploitation of the high surface area and mass diffusion, which should provide access to a broad range of new applications.

Results and Discussion

First, we synthesized the COF gels by mixing the corresponding aldehyde- (1,3,5 benzenetricarbaldehyde, **BTCA** or terephthalaldehyde, **PDA**) and amine- (1,3,5-tris(4-aminophenyl) benzene, **TAPB**, or 1,4-diaminobenzene, **PPDA**) monomers in glacial acetic acid (AcOH) with water (10 %, v/v) in a dialysis membrane at room temperature. The corresponding mixture was then left undisturbed in contact with additional AcOH at an oven at 25ºC for 5 days. Note that, although the formation of COF gels in other several organic solvents (*e.g.* dimethyl-sulfoxide or *m*-cresol)[23] had previously been described, after trying some of those, we ultimately chose AcOH because it enables the optimum solvent exchange process needed for the subsequent drying step in $scCO_2$ (see below). Moreover, we found that gelation does not require heating of the precursor solution, but that in order to be uniform, it did require the addition of 10 % of water (v/v). Additionally, although the COF gels had formed instantaneously, we incubated them at room temperature in AcOH for 5 days to enhance their porosity and crystallinity. Interestingly, we observed that shorter incubation times lead to a decrease in the crystallinity, while longer incubation times induce material degradation (Section S3, SI).

Next, we produced our low-density aerogels by drying the previously synthesized gels with $scCO_2$. This began with two solvent-exchange processes: one with tetrahydrofuran (THF), to remove unreacted monomers, and the other with ethanol (EtOH). Again, this is where the use of AcOH as solvent in the previous step had proved advantageous, as our attempts at solvent-exchange in COF gels that we had synthesized in dimethyl-sulfoxide or *m*-cresol, let to partial retention of those solvents and hampering the $scCO_2$ exchange. Importantly, we had to perform the solvent exchanges using a solvent gradient between them, *i.e.* THF *vs* EtOH, to prevent the collapse of the gel from possible solvent-structure interactions. Finally, exchange with subcritical CO_2(l) and supercritical CO_2 activation, by venting up *ca*. 8-10 bar h^{-1} to atmospheric pressure, gave rise to the three imine-based COF aerogels, which we named **TAPB-BTCA-AGCOF**, **PPDA-BTCA-AGCOF**, and **TAPB-PDA-AGCOF** (Scheme 1). The control of the venting caudal was critical in the formation of the monolithic COF aerogels, as uncontrolled venting led to the collapse of the monolithic COF structures.

We would like to highlight the importance of the $scCO_2$ drying process, as open-atmosphere drying of the COF gels led to the formation of COF xerogels (Section S2, S5, S6; SI), whose porous structures collapsed due to shrinking of the COF gel structure upon capillary strain of the solvent. We believe that this microstructural collapse was responsible both for a large loss in porosity and a decrease in the intensity in the powder X-ray diffraction (PXRD) peaks relative to the respective COF aerogels (*vide infra*). Moreover, it also leads to the appearance of a broad diffraction peak at ~20-25 ° in the PXRD, which we attributed to a partial collapse of the COF (Section S7, SI), thus corroborating results recently reported by Dichtel *et al.*[24]

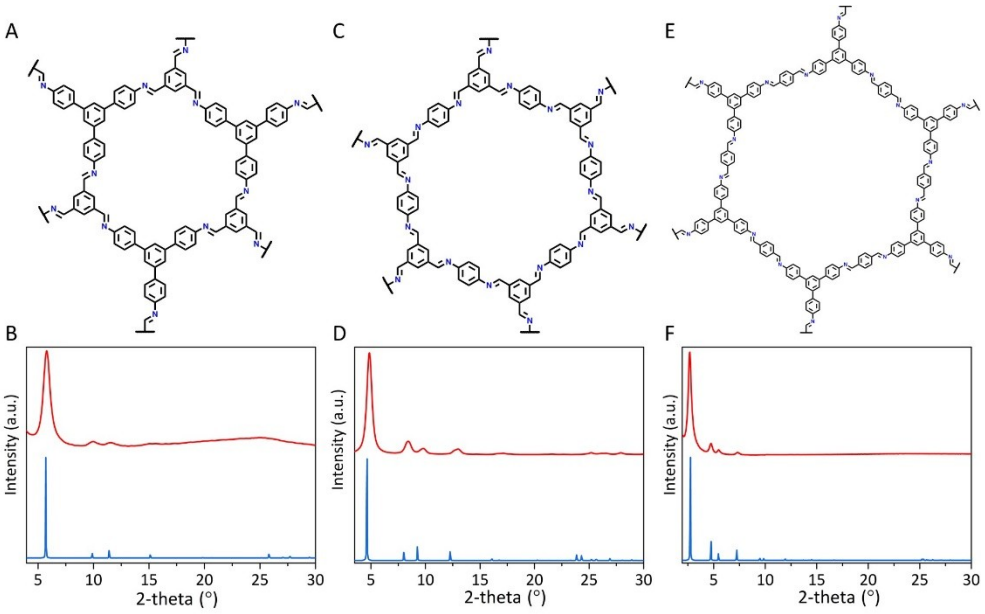

Figure 1. (A, C, E) Representation of the structures of the 2D imine-based **TAPB-BTCA** (A), **PPDA-BTCA** (B) and **TAPB-PDA** (C) COFs; and (B, D, F) PXRD patterns of the corresponding aerogels, showing the experimental (red lines) and corresponding simulated patterns (blue lines) for **TAPB-BTCA-AGCOF** (B), **PPDA-BTCA-AGCOF** (D) and **TAPB-PDA-AGCOF** (F).

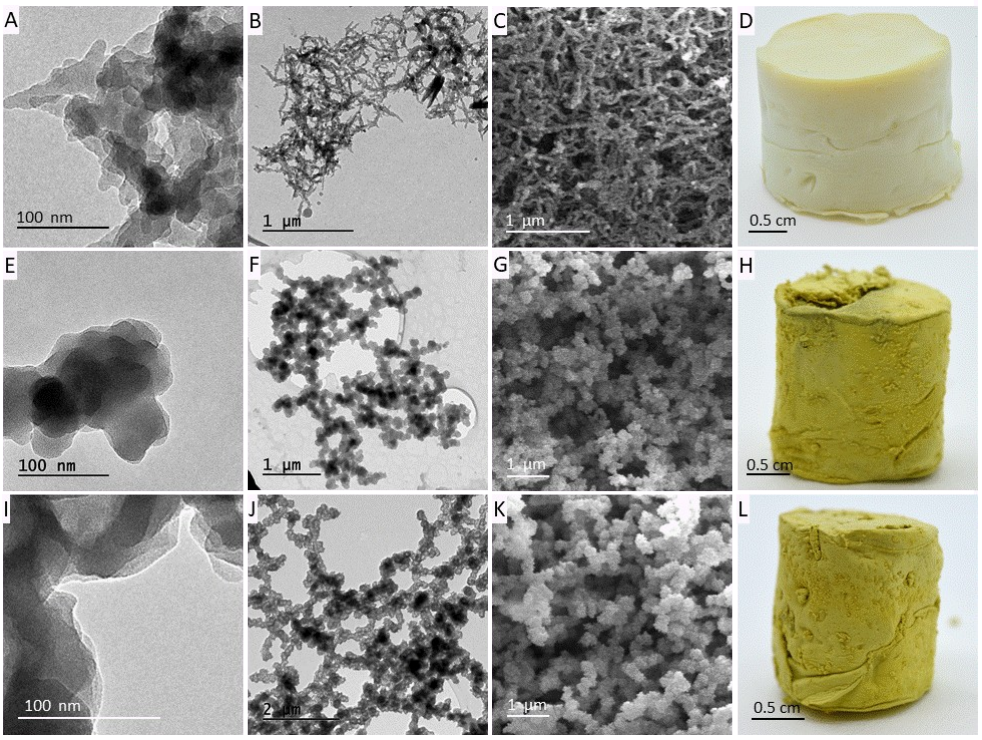

Figure 2. Transmission electron micrographs (A, B, E, F, I, J), scanning electron micrographs (C, G, K) and photographs (D, H, L) of **TAPB-BTCA-AGCOF** (A-D), **PPDA-BTCA-AGCOF** (E-H), and **TAPB-PDA-AGCOF** (I-L).

PXRD patterns of the three COF aerogels exhibited a good crystallinity, matched the simulated pattern of the AA-eclipsed stacking models, and were comparable with the PXRD patterns of their solvothermal counterparts.[25] Thus, **TAPB-BTCA-AGCOF** showed an intense peak at 5.7° corresponding to the (100) plane, along with the peaks at 9.9° and 11.5° attributed to the (110) and (200) reflections (Figure 1B). Similarly, **PPDA-BTCA-AGCOF** displayed the three peaks at 4.8°, 8.4°, and 9.8°, corresponding to the (100), (110), and (200) planes, respectively (Figure 1D). Also, **TAPB-PDA-AGCOF** showed the three peaks at 2.9°, 4.9°, and 5.6° attributed to the (100), (110), and (200) planes, respectively (Figure 1F). Altogether, these results agree with the formation of the expected COF structures based on ordered 2D layers.

We further characterized our COF aerogels by UV-vis absorption and emission spectroscopies (Section S4, SI), as well as Fourier transforms infrared (FT-IR) spectroscopy, which confirmed the typical imine (C=N) stretching band of at ~ 1620 cm^{-1} (Section S5, SI). Additionally, characteristic vibrations of the amino and carbonyl groups of the precursors were detected, with a substantial attenuation of the intensity at *ca.* ~1690 cm^{-1} (C=O, stretching bands) and ~3400 cm^{-1} (N-H, stretching bands), yet suggesting the presence of unreacted groups likely located at the defective edges of the COF nanolayers. Next, we turned to ^{13}C CP-MAS solid-state NMR, which corroborated the formation of imine bonds (characteristic imine carbon signal at ~156 ppm) and revealed a residual peak at ~190 ppm, which we assigned to the remaining aldehyde groups (Section S6, SI). Nevertheless, the rigorous quantification of unreactive defectives edges cannot be done spectroscopically. Finally, thermogravimetric analysis (TGA) under N_2 atmosphere showed that the COF-aerogels are thermally stable up to 500 ^0C (Section S8, SI). Next, we analyzed the microstructure of the COF aerogels by transmission electron microscopy (TEM) and electron microscopy scanning (SEM) (Sections S9 and S10, SI). All of the micrographs revealed a sponge-like architecture, in which COF nanolayers (Figures 2A, 2E, and 2I) are assembled into fiber-like structures (Figures 2B, 2F, and 2J), the interconnection of which gives rise to the formation of hierarchical meso- and macro-porous 3D aerogels (Figure 2). Statistical analyses of TEM images confirm nanolayer sizes of 30-45 nm for **TAPB-BTCA-AGCOF**; 60-100 nm for **PPDA-BTCA-AGCOF**; and 120-170 nm for **TAPB-PDA-AGCOF** (Section S10, SI).

To gain insight into the nature of the interlayer connections in the 3D aerogel structures, we closely analyzed the ^{13}C CP-MAS NMR spectrum of each of the activated COF aerogels together with its corresponding thermogravimetric results (Section S11, SI). We thus confirmed the presence of small quantities of AcOH. Therefore, we hypothesized that AcOH plays a significant role in the formation of the 3D networks in the aerogels – namely, by participating in the H-bonds that connect the amine and aldehydes groups between the layers. Accordingly, we reasoned that the presence of AcOH molecules throughout the aerogel formation enables the establishment of new imine condensation bonds at the grain boundaries between the COF-nanolayers within the structures, thereby leading to the formation of aggregates and, ultimately, of the 3D structures. Interestingly, a similar formation of free-standing membranes of the **TAPB-BTCA-COF** based on related interactions has already been reported.[26]

We found that the COF aerogels show extremely low densities (*ca*. 0.02 g cm^{-3}, Table S5). In fact, they are so light that a small chunk can rest comfortably atop the hairs of a dandelion (Figure 3A). We then assessed their mechanical stiffness through uniaxial quasi-static compression tests (Figure S29, Table S5). All samples behaved elastically below 25 % to 35 % strain, after which they were plastically compressed to a

maximum deformation of 90 %, yet without exhibiting failure. At this point, they demonstrated partial recovery, even at maximum deformation. Such compressive curves, usually described according to the typical behavior of an elastomeric foam with connected cells, comprise three regions. The first region (known as the Hookean region) corresponds to linear elasticity at low stresses and is dominated by cell-wall bending. The second region is a plateau of prolonged-collapse, whereby the stresses increase monotonically, implying elastic buckling of the wall. Finally, the third region comprises an area in which the stress rises steeply; here, the cells have almost completely collapsed, and further strain promotes the densification of the material (Section S12, SI).[27] These three stages have been observed in benchmark graphene-based aerogels.[28] However, in some studies, the Hookean region drastically decreases with the lowering of the density, in some cases even eventually disappearing.[28b] In fact, observation of the Hookean region demands a certain number of cell walls be aligned with the pressure axis in order to provide sufficient resistance to the stress; otherwise, only the other two regions are observed. This scenario is what we observed with our COF aerogels, whose compressive curves lack a Hookean region and whose deformation - even at extremely low values of stress - is dominated by elastic buckling (Figure 3C). The highly-porous aerogel microstructure has a stochastic distribution of widely and loosely-connected cavities separated by particles built up from the piling of a few 2D covalent sheets. Indeed, the basic 2D morphology of the COFs makes them very prone to buckling. The elastic moduli of the three COF aerogels are summarized in Figure 3B. Reflecting on the differences that we observed for the elastic modulus, we reasoned that there could be three possible explanations that are not mutually exclusive: i) the microstructure of the COF aerogels (including their density); ii) the shape and dimensions of the particles within the aerogel (*i.e.* the molecular structure); and iii) the air flowing away from the aerogel.

However, given the lack of significant differences in the particle size and density values, we hypothesized that the mechanical behavior of our COFs is strongly dominated by their 2D molecular features. For example, they can be arbitrarily decomposed into a rigid node (triple-branched benzene ring) and more-flexible extended linear connectors. As expected, the calculated elastic modulus followed the same ordering as the diameter of the void and the closely related length of the linear connector.

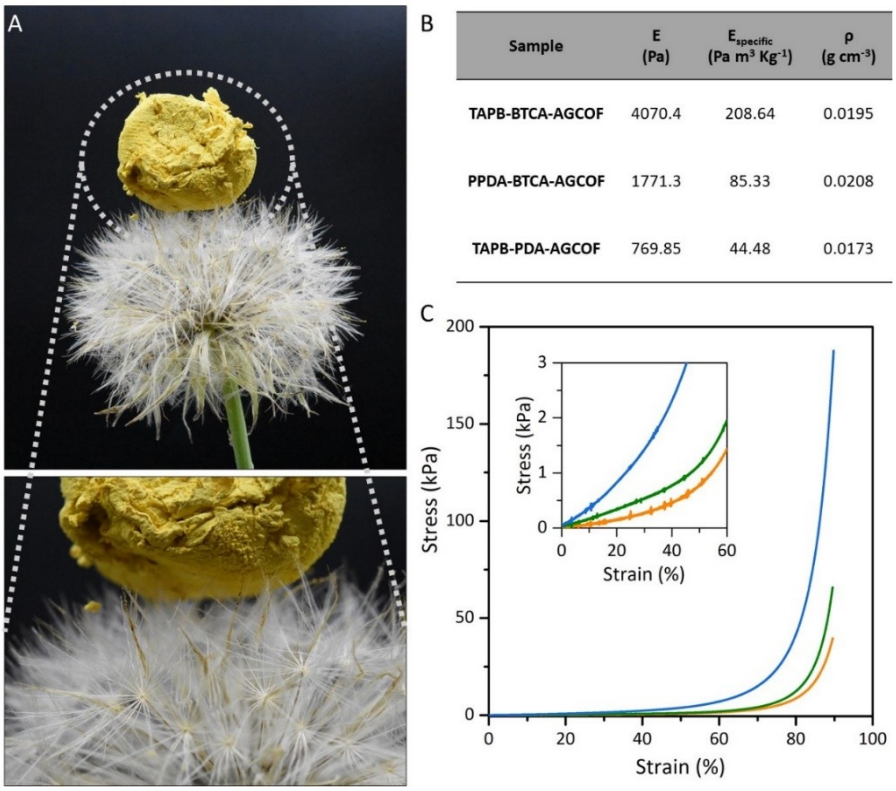

Sample	E (Pa)	$E_{specific}$ (Pa m^3 Kg^{-1})	ρ (g cm^{-3})
TAPB-BTCA-AGCOF	4070.4	208.64	0.0195
PPDA-BTCA-AGCOF	1771.3	85.33	0.0208
TAPB-PDA-AGCOF	769.85	44.48	0.0173

Figure 3. (A) The aerogels reported here have extremely low densities, as illustrated by this photo of a chunk of monolithic **TAPB-PDA-AGCOF** aerogel resting on top of dandelion hairs. (B) Calculated elastic modulus and density values for the three COF aerogels. (C) Compression-strain curves obtained for **TAPB-BTCA-AGCOF** (blue-line), **PPDA-BTCA-AGCOF** (green-line), and **TAPB-PDA-AGCOF** (yellow-line). Inset: zoom on the area of low-stress.

However, the density of rigid nodes per area within the sheet correlated nearly perfectly with the compressibility value, β (the inverse of the elastic modulus), in the form of $\beta = \frac{1}{E} = A - m C_{nodes}$, where A is related to the flexibility of the connector and m, to the rigidity of the node (Figure S32). As the chemical nature of the connectors is quite similar to an analogous single-to-double-bond ratio, we considered the A parameter to be the same for the three aerogels. As intuitively expected, this correlation indicates that as the concentration of rigid nodes within the sheet increases, the elastic modulus enhances. Regardless, the limited number of members in this novel family of COF-based aerogels indicates that verification of this apparent correlation will require further work.

Having characterized our COF aerogels extensively for diverse physicochemical and mechanical parameters, we then turned to functional testing of their permanent porosity by measuring their N_2 adsorption isotherms at 77 K. The isotherms for **TAPB-BTCA-AGCOF** and **PPDA-BTCA-COF** present a steep increase at low values of relative pressure, followed by a monotonic increase in the quantity adsorbed over 0.4 (Figure 4A and 4B); a trend typical of porous structures with a wide range of porosity. Detailed analyses of these adsorption isotherms by DFT revealed the presence of the pore cavities at 1.2 nm and 1.4 nm, which we assigned to the crystallographic pores of **TAPB-BTCA-AGCOF** and **PPDA-BTCA-AGCOF**,[10c, 24, 29] respectively. They also revealed the presence of additional disordered cavities as the cumulative pore volume monotonically increases above pore-width values greater than those of the crystallographic pores (Figures S34 and S37; Section S13, SI). In contrast, the adsorption isotherm of **TAPB-PDA-AGCOF** exhibits a hysteresis loop between the adsorption and desorption branches at low relative pressure (Figure 4C). Once the DFT method was applied, the cumulative pore size distribution (Figure S40) showed some porosity related to its crystallographic pores (3.3 nm), in addition to smaller pores in the range of to the so-called supermicropores, which we similarly attributed to interparticle aggregation or to a certain degree of interpenetration and other gate-opening phenomena, as previously observed in COF-300.[30]

From the aforementioned isotherms, we calculated Brunauer−Emmett−Teller (SA_{BET}) surface areas of 1146 $m^2 g^{-1}$ for **TAPB-BTCA-AGCOF**, 677 $m^2 g^{-1}$ for **PPDA-BTCA-COF**, and 2535 $m^2 g^{-1}$ for **TAPB-PDA-AGCOF**. These values, which are close to those found for their solvothermal counterparts,[10c, 24, 29] further confirm the quality of the COFs forming the aerogels. They also confirm the absence of precursors inside the inner porosity of the COFs, especially in the case of **TAPB-BTCA-AGCOF** and **TAPB-PDA-AGCOF**, corroborating our previous identification, by FT-IR spectroscopy, of amine and aldehyde groups as structural-functional groups. Moreover, taking into account the structural and microstructural porosity, we estimated a total porosity percentage of *ca*. 99 % for the three COF aerogels (Table S6). These values are slightly higher compared to other aerogels,[31] because in addition to the extrinsic/microstructural porosity, the intrinsic porosity of the COFs produces an enhancement of *ca*. 3-5 %.

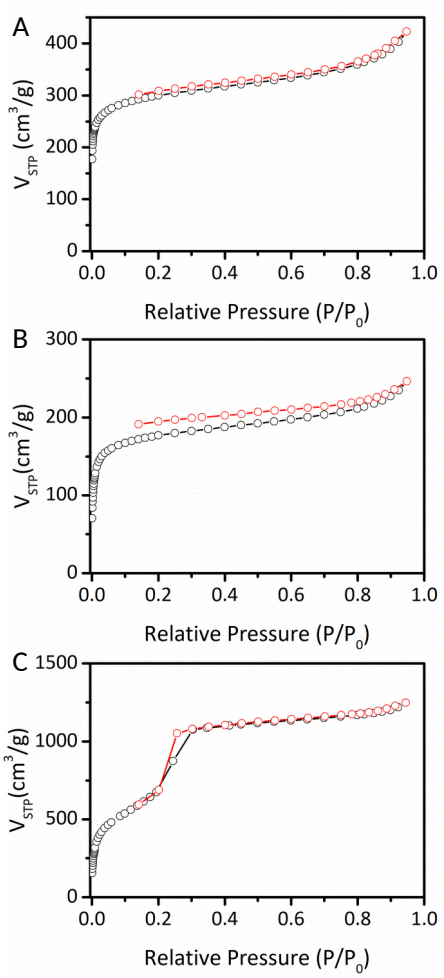

Figure 4. N_2 adsorption–desorption isotherms for (A) **TAPB-BTCA-AGCOF**, (B) **PPDA-BTCA-AGCOF**, and (C) **TAPB-PDA-AGCOF.** Adsorption branch in black, desorption branch in red.

Considering the low densities, hierarchical pore size, monolithic forms, hydrophobicity, and high BET surface areas (SA_{BET}) of our three COF aerogels, we were inspired to evaluate their performance as oil-scavengers. Thus, we tested the capacity of each aerogel to remove a model organic contaminant, such as toluene from water. Initially, Oil Red O dye (as a simple visual indicator) was dissolved in 1 mL toluene (10^{-2} M) and added to 30 mL of water. Afterward, each monolithic aerogel was placed in contact with the mixture for 1 min. Note that we used the COF-aerogels directly as oil-adsorbents, without any additional support (Figure 5A). After this time, the COF aerogels were removed, at which point they showed a characteristic red color confirming the successful adsorption of the Oil Red O dye/toluene solution. The aerogels were then dried under vacuum for 3 h, and the adsorbed Oil Red O dye/toluene solution was fully extracted with 20 mL of dichloromethane, from which a colorless monolithic aerogel was obtained, thus confirming the extraction of Oil Red O dye/toluene. Finally, the Oil Red O dye/toluene content in the dichloromethane was quantified by UV/vis absorption spectroscopy (Section S15, SI), from which we measured adsorption capacities of 24.7 g g^{-1} for **TAPB-BTCA-AGCOF**, 25.5 g g^{-1} for **PPDA-BTCA-AGCOF**, and 32.6 g g^{-1} for **TAPB-PDA-AGCOF** (Figure 5B). Remarkably, the toluene-removal capacity from water of our three COF aerogels is in the range of

other carbonaceous aerogel-type adsorbents reported to have excellent performance, including graphene aerogel, reduced graphene oxide (rGO) foam, and poly(1, 3, 5-triethynylbenzene) (PTEB) aerogel (Table S7). We also tested the adsorption kinetics of COF-aerogels (Figure S43), observing rapid adsorption of toluene that reaches its maximum in less than 1 minute.

Additionally, we evaluated the regeneration of the **TAPB-PDA-AGCOF** monolithic aerogel during ten consecutive adsorption-desorption cycles of toluene from contaminated water. In each cycle, the COF aerogel saturated with toluene was regenerated first using solvent exchange with dichloromethane, and then activating the sample under a nitrogen flow for 1 (Movie S1). Remarkably, the COF aerogel exhibited no loss of toluene-adsorption capacity over the ten cycles (Figure S44).

We reasoned that the macroporous structure and simple synthetic procedure used to produce the COF aerogels could enable the incorporation of other nanomaterials (*e.g.* nanoparticles) into the COF aerogels. Thus, we envisioned creating new composite materials that would combine the hierarchical porosity of the COF aerogels with additional functionalities of the integrated nanomaterials. As a proof-of-concept, we incorporated Fe_3O_4@rGO particles, which are magnetically and electrically-active, into the aerogel **TAPB-BTCA-AGCOF**, by following the same three-step method that we had used for the aerogel synthesis, except that we first dispersed Fe_3O_4@rGO nanoparticles into the **BTCA** solution by ultrasonication (15 min). The resultant monolithic composite, which we named **[Fe_3O_4@rGO]@TAPB-BTCA-AGCOF**, is shown in Figure 5C. Analyses by SEM and PXRD revealed the structure of the desired monolithic aerogel **TAPB-BTCA-AGCOF**, confirming that its synthesis had not been affected by the nanoparticles (Figure 5D and Figure S45). Moreover, the PXRD pattern confirmed the presence of the Fe_3O_4@rGO particles within the monolithic aerogel, which was further confirmed by elemental mapping by energy dispersive X-ray spectrometry (EDX), which revealed a highly uniform distribution of Fe and O atoms (Section S16, SI). Notably, the porosity of **[Fe_3O_4@rGO]@TAPB-BTCA-AGCOF** is retained, and its toluene-adsorption capacity, 24.4 g g^{-1}, similar to that of **TAPB-BTCA-AGCOF**.

We next sought to evaluate the electrical and magnetic properties of the **[Fe_3O_4@rGO]@TAPB-BTCA-AGCOF**. Firstly, we measured the electrical conductivity of **[Fe_3O_4@rGO]@TAPB-BTCA-AGCOF** at room temperature by the two-contacts method, using silver paint directly on its surface, from which we obtained a value of *ca.* 1.6×10^{-6} S cm^{-1} (Figure S47 and Table S8). Finally, we studied the magnetic properties of **[Fe_3O_4@rGO]@TAPB-BTCA-AGCOF** by exposing a monolithic aerogel to a magnet, which is rapidly attracted to it (Movie S2).

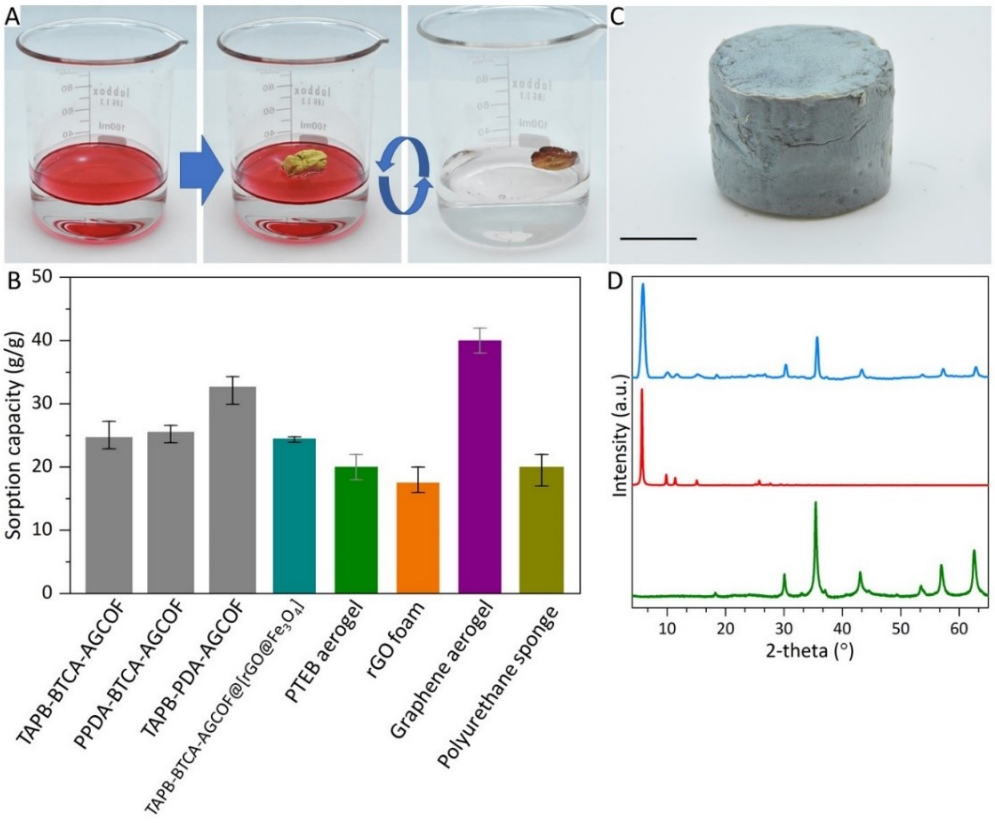

Figure 5. (A) Photographs of the removal experiment of toluene (dyed by Oil red O) from water using a **TAPB-PDA-AGCOF** monolith: (left) water contaminated with toluene (Oil Red O); (center) **TAPB-PDA-AGCOF** monolith on the top the toluene contaminated water; and (right) **TAPB-PDA-AGCOF** monolith on the top of the water after ten sorption-desorption cycles. B) Quantity of toluene removed by the COF aerogels (grey-bars) and other adsorbents; **[Fe_3O_4@rGO]@TAPB-BTCA-AGCOF** (turquoise-bar), PTEB aerogel (green-bar), rGO foam (orange-bar), graphene aerogel (purple-bar), and polyurethane sponge (olive-bar). (C) Photograph of **[Fe_3O_4@rGO]@TAPB-BTCA-AGCOF** (scale bar: 1 cm). (D) PXRD pattern of **[Fe_3O_4@rGO]@TAPB-BTCA-AGCOF** (blue-line), **Fe_3O_4@rGO** (green-line), and simulated (red-line).

Conclusion

We have reported here the synthesis of COF aerogels through a three-step method of sol-gel transition, solvent exchange, and, finally, activation with supercritical CO_2. These aerogels are formed, from gels, under very mild conditions without requiring binders and/or high pressures. This simple, low-cost, and green approach allows for the fabrication of ultralight aerogels of imine-based COF aerogels that have extremely low-densities (0.017 g cm^{-3} to 0.02 g cm^{-3}) and show hierarchical porosity with total porosity values of *ca*. 99 %, which are in the top-range of other aerogels.

Mechanically, the COF aerogels exhibit elastic behavior below 25 % to 35 % strain but become plastic after further compression to a maximum deformation of 90 %, albeit without exhibiting failure. Our mechanical studies indicate a particular relationship between the elastic modulus and rigidity of the corresponding molecular 2D structure.

To assess their adsorption capacity, we tested our COF aerogels for the uptake of toluene from an aqueous solution, for which they performed highly efficiently and with good recyclability. Finally, we demonstrated that the same three-step method could be used to synthesize COF aerogel/nanomaterial composites with multiple functionalities. As proof-of-concept, we synthesized a COF aerogel/iron-oxide nanoparticle composite with measurable electrical conductivity and magnetism. We are confident that our preliminary progress on COF aerogels facilitates access to a broad diversity of new COF aerogels and related composites, especially those with functionalities relevant to practical and industrial applications.

Acknowledgements

This work has been supported by the Spanish MINECO (PID2019-106268GB-C32, MAT2016-77608-C3-1-P, PCI2018-093081, PID2019-108028GB-C21, and RTI2018-095622-B-I00), the Catalan AGAUR (project 2017 SGR 238), and through the “María de Maeztu” Programme for Units of Excellence in R&D (CEX2018-000805-M). It was also funded by the CERCA Program/Generalitat de Catalunya. ICN2 is supported by the Severo Ochoa program from the Spanish MINECO (Grant No. SEV-2017-0706).

Keywords Covalent Organic Frameworks, Porous Materials, Aerogels, Functional Composites, Ultralight Monolithic aerogels.

[1] a) Z. Wang, S. Zhang, Y. Chen, Z. Zhang, S. Ma, *Chem. Soc. Rev.* **2020**, *49*, 708-735; b) S. Yuan, X. Li, J. Zhu, G. Zhang, P. Van Puyvelde, B. Van der Bruggen, *Chem. Soc. Rev.* **2019**, *48*, 2665-2681.

[2] a) K. W. Nam, S. S. Park, R. Dos Reis, V. P. Dravid, H. Kim, C. A. Mirkin, J. F. Stoddart, *Nat. Commun.* **2019**, *10*, 4948; b) L. Cao, Z. Lin, F. Peng, W. Wang, R. Huang, C. Wang, J. Yan, J. Liang, Z. Zhang, T. Zhang, L. Long, J. Sun, W. Lin, *Angew. Chem., Int. Ed.* **2016**, *55*, 4962-4966; c) U. Díaz, A. Corma, *Coord. Chem. Rev.* **2016**, *311*, 85-124; d) N. Huang, P. Wang, D. Jiang, *Nat. Rev. Mater.* **2016**, *1*, 16068.

[3] a) K. Geng, T. He, R. Liu, S. Dalapati, K. T. Tan, Z. Li, S. Tao, Y. Gong, Q. Jiang, D. Jiang, *Chem. Rev.* **2020**, *120*, 8814-8933; b) A. P. Cote, A. I. Benin, N. W. Ockwig, M. O'Keeffe, A. J. Matzger, O. M. Yaghi, *Science* **2005**, *310*, 1166-1170.

[4] C. S. Diercks, O. M. Yaghi, *Science* **2017**, *355*.

[5] a) A. Halder, S. Karak, M. Addicoat, S. Bera, A. Chakraborty, S. H. Kunjattu, P. Pachfule, T. Heine, R. Banerjee, *Angew. Chem., Int. Ed.* **2018**, *57*, 5797-5802; b) X. Li, C. Zhang, S. Cai, X. Lei, V. Altoe, F. Hong, J. J. Urban, J. Ciston, E. M. Chan, Y. Liu, *Nat. Commun.* **2018**, *9*, 2998.

[6] a) Y. Song, Q. Sun, B. Aguila, S. Ma, *Adv. Sci.* **2019**, *6*, 1801410; b) M. S. Lohse, T. Bein, *Adv. Funct. Mater.* **2018**, *28*, 1705553; c) W. Zhao, L. Xia, X. Liu, *CrystEngComm* **2018**, *20*, 1613-1634.

[7] a) T. Sun, J. Xie, W. Guo, D.-S. Li, Q. Zhang, *Adv. Energy Mater.* **2020**, *10*, 1904199; b) J. Li, X. Jing, Q. Li, S. Li, X. Gao, X. Feng, B. Wang, *Chem. Soc. Rev.* **2020**, *49*, 3565-3604.

[8] S. M. J. Rogge, A. Bavykina, J. Hajek, H. Garcia, A. I. Olivos-Suarez, A. Sepulveda-Escribano, A. Vimont, G. Clet, P. Bazin, F. Kapteijn, M. Daturi, E. V. Ramos-Fernandez, I. X. F. X. Llabres, V. Van Speybroeck, J. Gascon, *Chem. Soc. Rev.* **2017**, *46*, 3134-3184.

[9] a) D. W. Burke, C. Sun, I. Castano, N. C. Flanders, A. M. Evans, E. Vitaku, D. C. McLeod, R. H. Lambeth, L. X. Chen, N. C. Gianneschi, W. R. Dichtel, *Angew. Chem., Int. Ed.* **2020**, *59*, 5165-5171; b) Y. Ying, M. Tong, S. Ning, S. K. Ravi, S. B. Peh, S. C. Tan, S. J. Pennycook, D. Zhao, *J. Am. Chem. Soc.* **2020**, *142*, 4472-4480; c) W. Zhao, T.-P. Wang, J.-L. Wu, R.-P. Pan, X.-Y. Liu, X.-K. Liu, *Chin. J. Polym. Sci.* **2019**, *37*, 1045-1052; d) H. Wang, Z. Zeng, P. Xu, L. Li, G. Zeng, R. Xiao, Z. Tang, D. Huang, L. Tang, C. Lai, D. Jiang, Y. Liu, H. Yi, L. Qin, S. Ye, X. Ren, W. Tang, *Chem. Soc. Rev.* **2019**, *48*, 488-516; e) D. Rodriguez-San-Miguel, F. Zamora, *Chem. Soc. Rev.* **2019**, *48*, 4375-4386; f) Y. Zhao, L. Guo, F. Gandara, Y. Ma, Z. Liu, C. Zhu, H. Lyu, C. A. Trickett, E. A. Kapustin, O. Terasaki, O. M. Yaghi, *J. Am. Chem. Soc.* **2017**, *139*, 13166-13172.

[10] a) R. R. Liang, S. Y. Jiang, R. H. A, X. Zhao, *Chem. Soc. Rev.* **2020**, *49*, 3920-3951; b) L. Garzon-Tovar, J. Perez-Carvajal, A. Yazdi, J. Hernandez-Munoz, P. Tarazona, I. Imaz, F. Zamora, D. Maspoch, *Angew. Chem., Int. Ed.* **2019**, *58*, 9512-9516; c) G. Zhang, M. Tsujimoto, D. Packwood, N. T. Duong, Y. Nishiyama, K. Kadota, S. Kitagawa, S. Horike, *J. Am. Chem. Soc.* **2018**, *140*, 2602-2609; d) M. Seo, S. Kim, J. Oh, S. J. Kim, M. A. Hillmyer, *J. Am. Chem. Soc.* **2015**, *137*, 600-603.

[11] a) N. Han, Z. Zhang, H. Gao, Y. Qian, L. Tan, C. Yang, H. Zhang, Z. Cui, W. Li, X. Zhang, *ACS Appl. Mater. Interfaces* **2020**, *12*, 2926-2934; b) M. Zhang, L. Li, Q. Lin, M. Tang, Y. Wu, C. Ke, *J. Am. Chem. Soc.* **2019**, *141*, 5154-5158; c) Z. Liu, H. Wang, J. Ou, L. Chen, M. Ye, *J. Hazard. Mater.* **2018**, *355*, 145-153.

[12] S. Karak, K. Dey, A. Torris, A. Halder, S. Bera, F. Kanheerampockil, R. Banerjee, *J. Am. Chem. Soc.* **2019**, *141*, 7572-7581.

[13] B. Cai, V. Sayevich, N. Gaponik, A. Eychmuller, *Adv. Mater.* **2018**, *30*, 1707518.

[14] N. Hüsing, U. Schubert, *Angew. Chem., Int. Ed.* **1998**, *37*, 22-45.

[15] S. Karamikamkar, H. E. Naguib, C. B. Park, *Adv. Colloid Interface Sci.* **2020**, *276*, 102101.

[16] D. Vallejo-Sánchez, P. Amo-Ochoa, G. Beobide, O. Castillo, M. Fröba, F. Hoffmann, A. Luque, P. Ocón, S. Pérez-Yáñez, *Adv. Funct. Mater.* **2017**, *27*, 1605448.

[17] a) J. Zhang, L. Liu, H. Liu, M. Lin, S. Li, G. Ouyang, L. Chen, C.-Y. Su, *J. Mater. Chem. A* **2015**, *3*, 10990-10998; b) R. Du, N. Zhang, H. Xu, N. Mao, W. Duan, J. Wang, Q. Zhao, Z. Liu, J. Zhang, *Adv. Mater.* **2014**, *26*, 8053-8058.

[18] S. Zhao, W. J. Malfait, N. Guerrero-Alburquerque, M. M. Koebel, G. Nystrom, *Angew. Chem., Int. Ed.* **2018**, *57*, 7580-7608.

[19] a) S. M. F. Vilela, P. Salcedo-Abraira, L. Micheron, E. L. Solla, P. G. Yot, P. Horcajada, *Chem. Commun.* **2018**, *54*, 13088-13091; b) L. Li, S. Xiang, S. Cao, J. Zhang, G. Ouyang, L. Chen, C. Y. Su, *Nat. Commun.* **2013**, *4*, 1774; c) M. R. Lohe, M. Rose, S. Kaskel, *Chem. Commun.* **2009**, 6056-6058.

[20] A. Carne-Sanchez, G. A. Craig, P. Larpent, T. Hirose, M. Higuchi, S. Kitagawa, K. Matsuda, K. Urayama, S. Furukawa, *Nat. Commun.* **2018**, *9*, 2506.

[21] F. Li, L.-G. Ding, B.-J. Yao, N. Huang, J.-T. Li, Q.-J. Fu, Y.-B. Dong, *J. Mater. Chem. A* **2018**, *6*, 11140-11146.

[22] C. Li, J. Yang, P. Pachfule, S. Li, M. Y. Ye, J. Schmidt, A. Thomas, *Nat. Commun.* **2020**, *11*, 4712.

[23] A. de la Pena Ruigomez, D. Rodriguez-San-Miguel, K. C. Stylianou, M. Cavallini, D. Gentili, F. Liscio, S. Milita, O. M. Roscioni, M. L. Ruiz-Gonzalez, C. Carbonell, D. Maspoch, R. Mas-Balleste, J. L. Segura, F. Zamora, *Chem. - Eur. J.* **2015**, *21*, 10666-10670.

[24] C. H. Feriante, S. Jhulki, A. M. Evans, R. R. Dasari, K. Slicker, W. R. Dichtel, S. R. Marder, *Adv. Mater.* **2020**, *32*, 1905776.

[25] a) B. J. Smith, A. C. Overholts, N. Hwang, W. R. Dichtel, *Chem. Commun.* **2016**, *52*, 3690-3693; b) S. Y. Ding, J. Gao, Q. Wang, Y.

Zhang, W. G. Song, C. Y. Su, W. Wang, *J. Am. Chem. Soc.* **2011**, *133*, 19816-19822; c) J. Dong, Y. Wang, G. Liu, Y. Cheng, D. Zhao, *CrystEngComm* **2017**, *19*, 4899-4904.

[26] C. Montoro, D. Rodriguez-San-Miguel, E. Polo, R. Escudero-Cid, M. L. Ruiz-Gonzalez, J. A. R. Navarro, P. Ocon, F. Zamora, *J. Am. Chem. Soc.* **2017**, *139*, 10079-10086.

[27] L. J. Gibson, M. F. Ashby, *Cellular Solids: Structure and Properties*, 2nd ed., Cambridge University Press, Cambridge, **1997**.

[28] a) H. Yang, T. Zhang, M. Jiang, Y. Duan, J. Zhang, *J. Mater. Chem. A* **2015**, *3*, 19268-19272; b) H. Hu, Z. Zhao, W. Wan, Y. Gogotsi, J. Qiu, *Adv. Mater.* **2013**, *25*, 2219-2223; c) S. Nardecchia, D. Carriazo, M. L. Ferrer, M. C. Gutierrez, F. del Monte, *Chem. Soc. Rev.* **2013**, *42*, 794-830; d) X. Zhang, Z. Sui, B. Xu, S. Yue, Y. Luo, W. Zhan, B. Liu, *J. Mater. Chem.* **2011**, *21*, 6494-6497.

[29] J. A. Martin-Illan, D. Rodriguez-San-Miguel, C. Franco, I. Imaz, D. Maspoch, J. Puigmarti-Luis, F. Zamora, *Chem. Commun.* **2020**, *56*, 6704-6707.

[30] F. J. Uribe-Romo, J. R. Hunt, H. Furukawa, C. Klock, M. O'Keeffe, O. M. Yaghi, *J. Am. Chem. Soc.* **2009**, *131*, 4570-4571.

[31] T. Woignier, L. Duffours, *Gels* **2018**, *4*, 12.

Entry for the Table of Contents

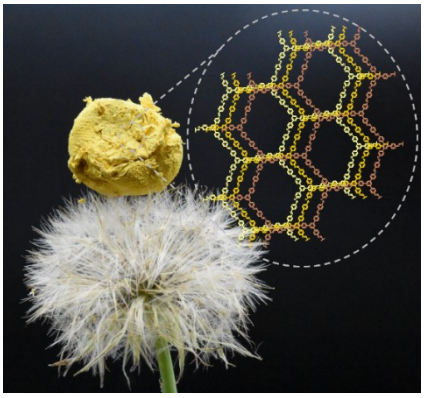

A three-step method produces COF aerogel monoliths, based on sol-gel transition, solvent-exchange, and supercritical CO_2 drying, in which 2D imine-based COF sheets link together to form hierarchical porous structures. The aerogels have extremely low densities, high porosity and mechanically behave as elastic or plastic materials under different strain. They show excellent absorption capacity (e.g. toluene uptake) with high removal efficiency.

Institute and/or researcher Twitter usernames: @fzamora0